Extended Abstract, 27th Conf. on Severe Local Storms, Amer. Meteor. Soc., 4-7 November 2014, Madison, WI

P161 A PARAMETRIC WIND-PRESSURE RELATIONSHIP FOR CONCENTRIC CYCLOSTROPHIC VORTICES

Vincent T. Wood[1], Robin L. Tanamachi[1], and Luther W. White[2]
[1]NOAA/OAR/National Severe Storms Laboratory, Norman, Oklahoma
[2]Department of Mathematics, University of Oklahoma, Norman, Oklahoma

1. INTRODUCTION

Karstens et al. (2010) summarized historical near-ground tornado measurements including maximum wind speeds and pressures as shown in their Table 1. The distributions of wind speeds and pressure deficits are of keen interest to engineers designing vital structures to survive tornado passage (e.g., Mishra et al. 2008; Haan et al. 2010; Yang et al. 2011). The measurements in that table, however, should be used with some caution for the following reasons. First, estimates of near-ground wind speed peaks and central pressure deficits provided by Davies-Jones and Kessler (1974) are based mostly on damage and thus have a large degree of uncertainty given known complexities in estimating wind speed from damage (Doswell et al. 2009). Second, the shapes of the radial profiles of tangential winds and the approximate radial distances at which the measured wind speed maxima occurred were either approximated or unknown. Wood and White (2013, hereafter WW13) showed that the sensitivity of central pressure deficit in an axisymmetric vortex core, via a cyclostrophic balance assumption, is strongly related to the choice of the free parameters that control the shapes of the radial profiles of tangential velocity. For instance, when compared to a Rankine[1] vortex, the parametrically constructed non-Rankine[2] vortices have a larger central pressure deficit. Third, in those studies in which *in situ* probes made near-ground pressure and wind measurements within close range of an intercepted tornado, no attempt was made to distinguish the measurements from the tornado from those of a possible background larger-scale vortex (e.g., a tornado cyclone or mesocyclone) in which the tornado was embedded. High-resolution mobile Doppler radar data collected by Marquis et al. (2008) and Wurman and Kosiba (2013) revealed complex vortex structures including quasi-concentric multiple wind field maxima (e.g., a tornado embedded in a tornado cyclone which was sometimes embedded in a larger-scale background vortex). Fourth, the sampling frequency of the mobile mesonet instruments (e.g., Karstens et al. 2010) is critical in determining whether true deficit pressure and maximum winds within close range of an intercepted tornado were captured or not. High (low) frequencies in the sampling would sufficiently (inadequately) resolve the characteristics of a tornado if the tornado's core passed directly over or nearby *in situ* probes. It is possible that some pressure deficit measurements are erroneous due to instrument damping and sluggish response (Davies-Jones 1986) because pressure gradients are very intense in tornadoes.

The objective of this study is to use the WW13 parametric tangential velocity profile model coupled with the cyclostrophic balance assumption to provide a diagnostic tool for parametrically constructing and estimating representative pressure deficit profiles deduced from a theoretical superposition of multiple-maxima tangential velocity profiles. These approximate profiles may resemble those in real tornadoes, tornado cyclones, and larger-scale background vortices. The balance is partitioned into separate pressure components that correspond to multiple-maxima cyclostrophic wind profiles in order to quantitatively evaluate the significant fluctuations in central pressure deficits. Finally, we present a few examples, some from VORTEX2, in which the parametrically constructed model is fitted to a tangential velocity profile derived from high-resolution Doppler radar data collected in a real sub-tornado-strength convective vortex (Tanamachi et al. 2013).

2. THE WOOD-WHITE PARAMETRIC MODEL

A simple parametric vortex may be modeled using the parametric tangential velocity (V) profile of Wood and White (2011, 2013). The profile for axisymmetric flow is expressed by

$$V(\beta;\mathbf{m}) = V_x \frac{(\mu_i-\mu_o)^\lambda \beta^{\mu_i}}{\left[\mu_i \beta^{(\mu_i-\mu_o)/\lambda} - \mu_o\right]^\lambda}, \ \mu_i \geq 1, \mu_o < 0, \lambda > 0. \quad (1)$$

The profile employs a model vector of five key parameters: $\mathbf{m} = (V_x, R_x, \mu_i, \mu_o, \lambda)^{\mathrm{T}}$, where V_x is the maximum tangential velocity that occurs at the core radius R_x, r is the radius from the vortex center, and $\beta \equiv r/R_x$ is the dimensionless radius. The three shape parameters (μ_i, μ_o, λ) are related to different shapes of the velocity profiles. The tangential velocity profile is defined by (i) the growth parameter μ_i, which predominantly dictates the inner (subscript *i*) profile near the vortex center; (ii) the decay parameter μ_o, which primarily governs the outer (subscript *o*) profile beyond the radius of the tangential velocity maximum, and (iii)

[1]The Rankine (Rankine 1882) vortex is characterized by a core of solid-body rotation [wherein tangential velocity (v) ~ radius (r)], surrounded by an outer region of potential flow (wherein $v \sim 1/r$).

[2]The non-Rankine vortex may be defined as a viscous vortex that exhibits a smooth transition between solid-body rotation and potential flow that encompasses the annular zone of the velocity maximum, resembling the Burgers-Rott (Burgers 1948; Rott 1958) tangential velocity profile.

Corresponding author address: Vincent T. Wood, National Severe Storms Laboratory, 120 David L. Boren Blvd., Norman, Oklahoma 73072, USA; e-mail: Vincent.Wood@noaa.gov

the size parameter λ, which controls the radial width of the velocity profile straddling the velocity maximum. In the formulation of (1), the definitions of μ_i and μ_o for the non-Rankine model are the same for the Rankine model. For example, when $\mu_i = 1$, the inner tangential velocity increases linearly from zero at the vortex center to a maximum value V_x at the core radius R_x. When $\mu_o = -1$, the outer velocity decreases with velocity being inversely proportional to distance from the center. The only difference between the Rankine and non-Rankine models is the shape of tangential velocity in the annular zone of tangential velocity maximum (i.e., sharply vs broadly peaked). As shown in the illustrative examples of WW13's Figs. 3 and 4, an increase in μ_i (μ_o) yields a central pressure rise (fall) by lowering (rising) the inner (outer) velocity profile inside (outside) the radius of the maximum tangential velocity. An increase in λ changes the tangential velocity profile from sharply to broadly peaked and simultaneously produces the corresponding central pressure fall.

Two factors that complicate the tangential velocity profiles within a few meters of the surface are friction and debris loading/centrifuging. The Wood-White parametric model does not account for these two factors which lie beyond the scope of this study.

3. WIND-PRESSURE RELATIONSHIP FOR CONCENTRIC CYCLOSTROPHIC VORTICIES

3.1 Cyclostrophic Wind Balance

In an axisymmetric vortex, the assumption of balance between dynamic pressure drop and wind speed, termed cyclostrophic balance, is given by

$$\frac{\partial P(r)}{\partial r} = \rho \frac{V_c^2(r)}{r} , \qquad (2)$$

where $V_c(r)$ is the cyclostrophic (tangential) velocity, $P(r)$ is the radial pressure perturbation with respect to the motionless base state at radial infinity, and ρ is the air density assumed to be horizontally constant (which is not strictly true). The pressure deficit ΔP is obtained by integrating (2) radially inward from an environmental pressure $P_e[= P(r \to \infty)]$ yields

$$\Delta P(r) = P(r) - P_e = \rho \int_{\infty}^{r} \frac{V_c^2(\tau)}{\tau} d\tau , \qquad (3)$$

where τ is a dummy variable for the integration. Integration of (3) is done numerically in all but simple cases; (3) involves the inward integral, which is calculated using the trapezoidal rule (e.g., Press et al. 1992, 125-126).

Given an idealized Rankine velocity distribution, ΔP at a vortex center is calculated as

$$\Delta P = -\rho V_x^2 . \qquad (4)$$

In (4), one's knowledge of either maximum tangential velocity above the surface boundary layer or central pressure deficit allows the other one to be crudely estimated. However, the utility of (4) is limited because (4) cannot be applied to multiple-maxima cyclostrophic wind profiles. This problem may be eliminated, as will be described in the subsequent subsections.

3.2 Partitioned Pressure-Wind Profiles for Multiple-Maxima Tangential Velocity Profiles

There have been numerous documented cases of quasi-concentric multiple wind field maxima in a variety of vortex configurations observed at finescale with mobile Doppler radars. Good examples of these maxima were provided in Marquis et al. (2008, their Figs. 2 and 3), Wurman and Kosiba (2013, their Figs. 8-12), and Wurman et al. (2014, their Figs. 2 and 3), among others, which displayed quasi-concentric multiple wind field peaks observed by mobile Doppler radars. The peaks were based on the velocity difference between the inbound and outbound Doppler velocity peaks) and core diameters (distances between these peaks). Sometimes, there is some difficulty in the subjective identification of conspicuous Doppler velocity couplets. Additionally, the center of a small circle (or ellipse) passing through the inbound and outbound Doppler velocity peaks may not be coincident with that of a large circle (or ellipse) passing through the outer peaks. To the best of the authors' knowledge, there have been no documented cases of more than three concentric tangential wind maxima in vortices scanned by mobile Doppler radars on a spatial scale of 10 km or less.

Fig. 1 presents the high-resolution Doppler radar reflectivity and velocity fields illustrating three concentric Doppler velocity peaks through the centers of the vortex signatures observed by RaXPol (a rapid-scan, polarimetric mobile radar) in southern El Reno, Oklahoma on 31 May 2013 (Pazmany et al. 2013; Snyder and Bluestein 2014). The definitions of *primary*, *secondary* and *tertiary* vortices are discussed in the next subsection.

In view of the above, the triple concentric vortex structure can be considered as a triple vortex composed of the first, second and third vortex configurations. We now show that the hypothesis on a three-vortex composite in the tangential velocity profiles enables the description of complex tangential velocity distributions. By isolating the primary tangential wind profile (V_p) from the secondary (V_s) and tertiary (V_t) tangential velocity profiles, the total cyclostrophic wind V_c profile in (1) may be partitioned into the V_p, V_s and V_t velocity components:

$$V_c(r) = V_p(\beta_p; \mathbf{m}_p) + V_s(\beta_s; \mathbf{m}_s) + V_t(\beta_t; \mathbf{m}_t) , \qquad (5)$$

where the subscripts (*p, s, t*), respectively, represent the primary, secondary and tertiary components. The V_p, V_s and V_t profiles each may be modeled using at least one wind profile in (1), given by

$$V_p(\beta_p; \mathbf{m}_p) = V_{px} \frac{(\mu_{pi} - \mu_{po})^{\lambda_p} \beta_p^{\mu_{pi}}}{\left[\mu_{pi}\beta_p^{(\mu_{pi}-\mu_{po})/\lambda_p} - \mu_{po}\right]^{\lambda_p}} , \qquad (6a)$$

$$V_s(\beta_s; \mathbf{m}_s) = V_{sx} \frac{(\mu_{si} - \mu_{so})^{\lambda_s} \beta_s^{\mu_{si}}}{\left[\mu_{si}\beta_s^{(\mu_{si}-\mu_{so})/\lambda_s} - \mu_{so}\right]^{\lambda_s}} , \qquad (6b)$$

and

$$V_t(\beta_t; \mathbf{m}_t) = V_{tx} \frac{(\mu_{ti} - \mu_{to})^{\lambda_t} \beta_t^{\mu_{ti}}}{\left[\mu_{ti}\beta_t^{(\mu_{ti}-\mu_{to})/\lambda_t} - \mu_{to}\right]^{\lambda_t}} . \qquad (6c)$$

Here, $\beta_p \equiv r/R_{px}$, $\beta_s \equiv r/R_{sx}$, and $\beta_t \equiv r/R_{tx}$ are, respectively, the dimensionless radii of the primary, secondary and tertiary profiles of tangential velocities. In (6), we need to convey that the vortices are ordered

not in order of radius of maximum wind, but in order of the magnitude of the maximum wind.

Fig. 2 illustrates the azimuthal profiles of Doppler velocity passing through the signature centers at approximately 5 km from the RaXPol. The presence of a weak tertiary vortex in Fig. 1 is questionable because it is difficult to subjectively identify a prominent area of inbound Doppler velocity minima to the south and outside of the secondary vortex. It appears that the Doppler velocity couplet of the tertiary vortex is not well pronounced as other couplets of the primary and secondary vortices.

To begin investigation of a triple vortex structure simulation, it is assumed that the centers of three perfect circles representing different model core diameters are coincident with one another. Substitution of (5) into (3) and manipulation of some variables yield the total partitioned pressure deficit $\Delta P_{tot}(r)$:

$$\Delta P_{tot}(r) = \Delta P_p(r) + \Delta P_s(r) + \Delta P_t(r)\ , \qquad (7)$$

where the partitioned pressure deficit components are expressed by

$$\Delta P_p(r) = \rho \int_{\infty}^{r} \left[\frac{V_p^2(\tau)}{\tau} + \frac{V_p(\tau)V_s(\tau)}{\tau} + \frac{V_p(\tau)V_t(\tau)}{\tau}\right] d\tau\ , \quad (8a)$$

$$\Delta P_s(r) = \rho \int_{\infty}^{r} \left[\frac{V_s^2(\tau)}{\tau} + \frac{V_s(\tau)V_p(\tau)}{\tau} + \frac{V_s(\tau)V_t(\tau)}{\tau}\right] d\tau\ , \quad (8b)$$

and $\Delta P_t(r) = \rho \int_{\infty}^{r} \left[\frac{V_t^2(\tau)}{\tau} + \frac{V_t(\tau)V_p(\tau)}{\tau} + \frac{V_t(\tau)V_s(\tau)}{\tau}\right] d\tau\ .$ (8c)

In (7), each partitioned pressure deficit component is assumed to attain the cyclostrophic balance which is accepted generally as a good approximation for each given vortex above the surface boundary layer. On the right-hand side of (8a), V_p^2 contributes most to the primary pressure deficit ΔP_p. The product of V_p and V_s partially contributes to ΔP_p only if there is a secondary tangential wind maximum ($V_{sx} \neq 0$) in the radial profile of V_s. Likewise, the product of V_p and V_t partially contributes (though to a lesser extent) to ΔP_p only if a tertiary tangential wind maximum ($V_{tx} \neq 0$) occurs in the radial profile of V_t. On the right-hand side of (8b), V_s^2 mainly contributes to the secondary pressure deficit ΔP_s, while the products $V_s V_p$ and $V_s V_t$ each play a minor in modulating ΔP_s, provided that the primary and tertiary tangential velocity maxima are present (i.e., V_{px} and $V_{tx} \neq 0$. An analogous description can be applied to (8c). In later sections, the relative contributions of V_p, V_s and V_t to the total pressure deficit ΔP_{tot} in (7) and (8) are explored and compared to elucidate the role of the partitioned tangential velocity profiles in the physical behavior of the corresponding pressure deficits at the vortex center.

4. PARAMETRIC PRESSURE-WIND PROFILE SIMULATION RESULTS

This section uses a simple vortex simulator to provide what each input parameter ($V_x, R_x, \mu_i, \mu_o, \lambda$) may be able to deduce about the primary, secondary and tertiary cyclostrophic vortices in terms of intensity. Intensity is measured by the central pressure deficit or maximum tangential velocity in the vortex core (WW13). We use the central pressure deficit as a proxy for intensity because it is our interest to investigate how a change in the shape and distribution of tangential wind directly affects intensity when comparing against the radial distributions of a "reference" Rankine (or non-Rankine) vortex's tangential velocity and pressure deficit. Note that the "reference" vortex refers to the primary vortex in the absence of external vortices (i.e., secondary and tertiary vortices). Furthermore, we compare cases by varying one parameter while keeping other parameters unchanged in the radial distributions of the secondary vortex's tangential velocity and pressure deficit (e.g., Table 1). These changes in parameter values are relative to the reference Rankine vortex in which the input parameter values are fixed. Finally, we present a detailed discussion on the manner in which the radial profiles of the secondary vortex's tangential velocity and pressure deficit are varied and compared to those of the reference Rankine vortex. Our approach was similar to that of Knaff et al. (2011), WW13, and Wood et al. 2013)

4.1 Vortex with Single-Maximum Tangential Wind

To begin with a reference Rankine vortex, we find that the radial distributions of tangential velocity and pressure deficit are calculated from (5)-(8) by setting V_{sx}, $V_{tx} = 0$ in (6b,c) and ΔP_s, $\Delta P_t = 0$ in (8b,c) and are given by

$$V_c(r) = V_p(r) \equiv V_{ref}(r), \qquad (9)$$

$$\Delta P_{tot}(r) = \Delta P_p(r) \equiv \Delta P_{ref}(r). \qquad (10)$$

Here, the parametric vortex model coincides with the reference Rankine vortex model by setting $\mu_{pi} = 1$ and $\mu_{po} = -1$ in (6a) and taking the limit of (6a) as $\lambda_p \to 0$. This is given by

$$V_{ref}(r) = V_{px}\left\{\lim_{\lambda_p \to 0} \frac{\left(\mu_{pi} - \mu_{po}\right)^{\lambda_p} \beta_p^{\mu_{pi}}}{\left[\mu_{pi}\beta_p^{(\mu_{pi}-\mu_{po})/\lambda_p} - \mu_{po}\right]^{\lambda_p}}\right\}$$

$$= \begin{cases} V_{px}\beta_p, & \beta_p \le 1, \\ \frac{V_{px}}{\beta_p}, & \beta_p > 1. \end{cases} \qquad (11)$$

Note that the subscript ref represents the reference Rankine vortex. The red curve in Fig. 3a represents the tangential velocity of a classic Rankine vortex that has long been of interest to scientists, because it is believed to approximate naturally occurring atmospheric vortices.

A reference pressure deficit ΔP_{ref} for the reference Rankine vortex is derived by incorporating V_{ref} into (3) and integrating the result inward radially in a piecewise manner (WW13). Thus, ΔP_{ref} is obtained as

$$\Delta P_{ref}(r) = \begin{cases} \rho V_{px}^2 \left(\frac{\beta_p^{2\mu_{pi}}}{2\mu_{pi}} + \frac{\mu_{pi}-\mu_{po}}{2\mu_{pi}\mu_{po}}\right), & \beta_p \le 1 \\ \rho V_{px}^2 \left(\frac{\beta_p^{2\mu_{po}}}{2\mu_{po}}\right), & \beta_p > 1 \end{cases}. \qquad (12)$$

By setting $\mu_{pi} = 1$ and $\mu_{po} = -1$ in (12), ΔP_{ref} at the vortex center ($\beta_p = 0$) is simplified to (4). The reference Rankine vortex is assumed to be a steady-state tornado vortex having its maximum tangential velocity of 100 m s^{-1} at its core radius of 200 m. As a consequence, the radial profile of ΔP_{ref} is calculated and plotted by the

purple curve in Figs. 3b, d. The reference central pressure deficit is -117 hPa. As will be shown in the subsequent subsection, we seek to determine how the wind structural changes are related to variations in intensity and size when the steady-state tornado is embedded in an evolving tornado cyclone (representing a secondary vortex) in terms of varying secondary tangential velocity profiles. The evolving tornado cyclone will be analyzed in relation to changing each of five key parameters for the given tornado cyclone.

4.2 Vortices with Dual-Maxima Tangential Winds

A tornado embedded in a tornado cyclone may be modeled by (a) setting $V_{tx} = 0$ in Eq. (6c) and (b) defining selected input parameters for initializing the primary and secondary vortices (Table 1). The input parameters pertaining to the reference Rankine vortex (representing the steady-state tornado) remain unchanged for comparison. When a new radial profile of the secondary tangential velocity (V_s) is added to the primary tangential velocity (V_p) profile of the reference vortex, the radial distributions of tangential velocity and pressure deficit are given by

$$V_c(r) = V_p(r) + V_s(r)\ , \qquad (13)$$

$$\Delta P_{tot}(r) = \Delta P_p(r) + \Delta P_s(r)\ , \qquad (14)$$

where

$$\Delta P_p(r) = \rho \int_{\infty}^{r} \left[\frac{V_p^2(\tau)}{\tau} + \frac{V_p(\tau)V_s(\tau)}{\tau}\right] d\tau\ , \qquad (15a)$$

$$\Delta P_s(r) = \rho \int_{\infty}^{r} \left[\frac{V_s^2(\tau)}{\tau} + \frac{V_s(\tau)V_p(\tau)}{\tau}\right] d\tau\ . \qquad (15b)$$

Eq. (13) is calculated from (6a, b), using the defined input parameters in Table 1.

When the secondary vortex is added to the reference Rankine vortex, a new radial profile of tangential velocity is created (black curve in Fig. 3a). The profile produces a change in the radial profile of the reference pressure deficit. The central pressure deficit at the vortex center has fallen from -117 hPa to -127 hPa, even though the reference vortex remains unchanged (Fig. 3b). This is because the product of V_p and V_s partially contributes an extra -10 hPa to ΔP_p [see Eq. (15a)] at the vortex center. A small secondary central pressure deficit (ΔP_s = -17 hPa, blue curve in Fig. 3b) is generated, corresponding to the added radial profile of the secondary vortex's tangential velocity (blue curve in Fig. 3a). Thus, the secondary central pressure deficit contributes an extra -17 hPa to the primary vortex's central pressure deficit of -127 hPa. This contribution results in the total central pressure deficit (ΔP_{tot} = -144 hPa), comparing to the reference central pressure deficit (ΔP_{ref} = -117 hPa).

Let us suppose that the tornado cyclone's tangential velocity maximum (represented by the secondary vortex A's V_{sx} in Table 1) increases from 25 to 50 m s^{-1}, as indicated by transforming the blue dashed curve to the blue solid curve in Fig. 3c. As expected, such an increase in tangential velocity peak is strongly correlated with vortex intensity and pressure fall (-186 hPa in Fig. 3d) when other free parameters of the secondary vortex A are held constant (Table 1).

Lee and Wurman (2005) and Wood and White (2013) showed that the size of any atmospheric vortex is irrelevant in calculating the central pressure deficit. The central pressure deficit of a single vortex appears to be relatively insensitive to variations in R_x. However, the total pressure deficit ΔP_{tot} in a dual-vortex configuration is seen to change its magnitude from -144 to -156 hPa when the secondary tornado cyclone (vortex B) contracts the 2-km core radius R_{sx} to a 1-km core radius (see Table 1), while at the same time, the core radius of the reference Rankine vortex remains unchanged (Fig. 4).

Now that we comprehend how the different V_{sx} and R_{sx} values control the total central pressure deficit, we further explore the role of the growth parameter (μ_{si}) of the secondary vortex C. Figs. 5c, d illustrate how varying the μ_{si} value can have impact on the behavior of the pressure deficit profiles. At given values of other free parameters (Table 1), a transition from the right half of a V-shaped profile (blue dashed curve in Fig. 5c) to the right half of a U-shaped profile (blue solid curve) of the secondary vortex C's tangential velocity produces a change in the corresponding pressure deficit profiles (Figs. 5b, d) as μ_{si} progresses from 1.0 to 5.0. At the same time, ΔP_s has risen from -17 to -7 hPa. Between the vortex center and 2.0 km from the center, the secondary vortex C pressure structure (blue curve in Fig. 5d) has a flat deficit for $\mu_{si} > 1.0$. An increase in μ_{si} tends to produce a decrease in vortex intensity and a rise in the central pressure deficit. At the same time, ΔP_{tot} = -144 hPa is reduced to -127 hPa.

In the last subsection, the role of μ_{si} in the behavior of the radial distributions of the secondary vortex C's tangential velocity and corresponding pressure deficit has been discussed. We now investigate how varying a decay μ_{so} parameter (Table 1) in a secondary vortex D produces a change in the radial distributions of pressure deficits. Increasing μ_{so} produces a slow decay of the outer secondary tangential velocity (V_s) and causes the central pressure deficit to fall slowly, thereby increasing vortex intensity slightly (Fig. 6).

In contrast to the tangential velocity and pressure deficit profiles of the secondary Rankine vortex, the secondary non-Rankine vortex (vortex E in Table 1 and Fig. 7) admits a great variety of the tangential velocity and pressure deficit distributions depending heavily upon the values of the size parameter λ_s. As λ_s progresses from ~0 to 1.0, the secondary Rankine vortex E evolves to the secondary non-Rankine vortex E by transitioning the sharply peaked profile (blue dashed curve in Fig. 7c) to a broadly peaked profile (blue solid curve) in the annular zone of tangential velocity maximum. The evolving pressure deficit distribution produced by an increase in λ_s is lowered as it departs from that of the secondary Rankine vortex E (Fig. 7b), thereby producing an increase in vortex intensity.

Let us hypothesize that the primary Rankine vortex undergoes a change to a primary non-Rankine vortex while at the same time, the secondary Rankine vortex remains unchanged. The change in λ_p and other unvaried parameters are shown in Table 2 for vortex F.

Such a change produces a big drop in the central pressure deficits (Fig. 8d). On the right-hand side of (8a), V_p^2 contributes a great deal to such a drop.

4.3 Vortices with Triple-Maxima Tangential Winds

Wurman and Kosiba (2013) documented rare cases of concentric vortex signatures with triple tangential wind maxima observed by mobile Doppler radars. In this subsection, we present a brief discussion on the manner in which the radial profiles of tertiary tangential velocity and pressure deficit are added to the radial profiles of pre-existing primary and secondary tangential velocities and pressure deficits. To reproduce this tertiary vortex configuration, we use (5)-(8) to parametrically construct a weak, larger-scale background vortex. Let us assume the input parameters for initializing the tertiary Rankine tangential velocity (Table 3). Other initial conditions for specifying the primary and secondary Rankine vortices are the same as those in Figs. 3a, b (Table 1). With given input parameters for the three individual vortices, the total pressure deficits in (7)-(8) can be calculated.

Figure 9 illustrates radial distributions of concentric triple-maxima cyclostrophic tangential velocities and pressure deficits. As previously discussed, the combined V_p, V_s and V_t profiles on the right-hand side of (8) much more contribute to the primary, secondary and tertiary pressure deficits than do the combined V_p and V_s profiles to the primary and secondary pressure deficits. It is evident that the triple concentric Rankine vortex configuration has a larger central pressure deficit than does the dual concentric Rankine vortex configuration (Fig. 9b, d). If this vortex configuration were to evolve to the triple concentric non-Rankine vortex configuration (i.e., increasing the radial width of tangential velocity profile that encompasses the maximum), the latter configuration would have resulted in much greater central pressure falls than would the former configuration.

5. CASE STUDIES

5.1 Doppler Radar Observation of the Prospect Valley, Colorado Sub-Tornado-Strength, Convective Vortex of 26 May 2010 during VORTEX2

Tanamachi et al. (2013) described the collection of high-resolution, W-band Doppler radar data in a sub-tornado-strength, convective vortex (SCV) that occurred near Prospect Valley, Colorado on 26 May 2010 as part of the Second Verification of the Origins of Rotation in Tornadoes Experiment (VORTEX2) field campaign. A Ground-Based Velocity Track Display (GBVTD; Lee et al. 1999) analysis of Doppler velocity observations of the SCV produced the vortex-relative, asymmetric azimuthal velocities (sum of wavenumbers 0-3) at 2236:31, 2236:48, and 2237:06 UTC (Fig. 10). The tangential wind patterns of the asymmetric SCV display more complex structure than their axisymmetric counterparts (wavenumber 0), resulting from the effect of wavenumbers 0-3 at different azimuths and radii where the maximum tangential winds occur (e.g., Lee et al. 1999).

The radial distributions of the GBVTD-analyzed mean tangential wind (wavenumber 0) are presented in Fig. 11. At 2236:31 UTC, two GBVTD-analyzed azimuthally averaged tangential wind maxima, respectively, are 11.7 m s^{-1} located at 60 m and 8.9 m s^{-1} at approximately 300 m from the SCV center, indicative of the dual concentric vortex configuration consisting of the primary and secondary vortices. The radial profile of the dual-maxima tangential wind of the axisymmetric SCV changes to the radial profiles of the single-maximum tangential wind at 2236:48 and 2237:06 UTC (Fig. 11).

We seek to examine the parametric tangential wind profile's realism by assessing how well the parametric Wood-White parametric model, coupled with the cyclostrophic balance assumption, is able to produce the complex profiles of pressure deficits deduced from the Doppler radar-derived tangential wind output (Fig. 11). The Levenberg-Marquardt (LM) (Levenberg 1944; Marquardt 1963) optimization method is employed, which is a standard technique used to solve unconstrained nonlinear least squares problems for curve-fitting applications (e.g., WW13). The algorithm for implementing the LM method was described in Press et al. (1992).

A procedure, whereby we can reasonably estimate the dual-maximum tangential wind profiles, consists of the following basic steps with the aid of Fig. 12.

(a) To isolate a primary GBVTD-analyzed mean tangential wind profile from a secondary GBVTD-analyzed mean tangential wind profile, it is determined that the primary profile should be terminated just before the deficit profile between the locations of V_{px} and V_{sx}, as indicated by a blue dotted curve in Fig. 12.

(b) Scan through the primary profile of tangential wind until the first two model parameters (V_{px} and R_{px}) are found and defined as the initial guesses (as indicated by the intersection of dashed horizontal and vertical lines).

(c) Use this azimuthally averaged tangential wind speed ($\bar{V}_T$) profile as input to the minimization calculation in the LM algorithm.

(d) Examine the inner and outer profiles, as well as the the shape profile encompassing the wind maximum, before making initial guesses of the model parameters (μ_{pi}, μ_{po}, and λ_p).

(e) Minimize a cost function over the model vector of five key parameters $\mathbf{m_p} = \left(V_{px},\ R_{px},\ \mu_{pi},\ \mu_{po},\ \lambda_p\right)^{\mathrm{T}}$; the function is differentiable with respect to $\mathbf{m}_p$.

(f) If convergence fails, then make some adjustments of the model parameters before repeating steps (d) and (e).

(g) When convergence is achieved, finalize and compute the fitted model parameters in Eq. (6a) for plotting the primary profile (black curve in Fig. 12).

(h) Calculate the root-mean square (RMS) error and correlation coefficient (CC) value between the observed and fitted (primary) profiles, as shown in Table 4.
(i) Subtract the primary profile (V_p) from the observed profile (blue solid curve) to obtain a secondary profile (red solid curve).
(j) Determine the first two initial guesses (V_{sx} and R_{sx}) of the secondary model parameters by repeating step (b).
(k) Repeat steps (b) through (h) for generating the secondary fitted profile.
(l) Add the fitted secondary profile to the fitted primary profile (gray curve in Fig. 12).
(m) Use the fitted parameters to integrate the pressure deficit in (14)-(15) inward radially before plotting the deduced profiles of pressure deficit (Fig. 13).

Steps (a) through (m) are repeated for the next two observed profiles at 2236:48 and 2237:06 UTC (Fig. 11). The fitted model parameters generated by the LM algorithm are shown in Table 4. Having the fitted parameters available, we used (13), via (6a, b), to parametrically construct the radial distributions of the primary and secondary tangential velocities (Fig. 13a) and also (15) to integrate the pressure deficit inward radially to reproduce radial profiles of primary and secondary pressure deficits (Fig. 13b). As a consequence, the overall radial distributions of cyclostrophic wind and deduced pressure deficit in the dual-vortex configuration are produced (black curves). At the vortex center, the deficit pressure deficit is -3.14 hPa. Without the presence of the secondary vortex, a dynamic pressure drop would have been weak (the purple ΔP_{ref} curve) with its magnitude of -2.29 hPa at the vortex center.

Vortex morphology seems to change quickly between 2236:31 and 2236:48 UTC, as comparison between Figs. 13 and 14 illustrates. An increase in the fitted parameter λ_p (i.e., from $\lambda_p = 0.69$ to $\lambda_p = 2.21$ in Table 4) causes the radial profile of the primary tangential velocity encompassing the velocity maximum to widen suddenly at a given velocity level, thereby producing a prominent central pressure drop from $\Delta P_p =$ -2.49 to -3.83 hPa. Two other fitted parameters (μ_{pi} and μ_{po}), also in Table 4, do not change significantly.

Asymmetries in the GBVTD-analyzed tangential wind fields are noticeably changed from 2236:31 to 2237:06 UTC (Fig. 11), particularly in the 100-km radius. Maximum GBVTD-analyzed, asymmetric tangential velocities are reduced, while at the same time, maximum and deficit GBVTD-analyzed, asymmetric tangential velocities are increased at a larger radius from the vortex center. The changes result in the radial profiles of GBVTD-analyzed mean tangential velocities (Fig. 11). At 2236:48 UTC, the total pressure deficit of -4.21 hPa (Fig. 14b) is reduced to -3.76 hPa at 2237:06 UTC (Fig. 15b). At the same time, the secondary vortex is gradually disappeared. It is well known that tornadoes (and presumably SCVs) evolve on very short time scales (perhaps 1 s or less). It is suggested that angular momentum diffused radially outward in time between 2236:31 and 2237:06 UTC.

6. CONCLUSIONS

The Wood and White parametric tangential velocity profile model coupled with the cyclostrophic balance assumption offered a diagnostic tool for parametrically constructing and estimating representative pressure deficit profiles deduced from a theoretical superposition of multiple-maxima tangential velocity profiles as well as from the fitted, GBVTD-analyzed tangential velocity profiles of the Prospect Valley, Colorado SCVs of 26 May 2010. The main conclusions of this study are as follows:

1) The shape parameters (μ_i, μ_o, λ) each play an important role in modulating various portions of each radial profile of the tangential velocity. As described by WW13, the μ_i (μ_o) parameter primarily controls the inner (outer) profile near a vortex center (beyond the radius at which the tangential velocity peak occurs). The λ parameter mainly determines the radial width of the profile spanning the maximum. Each parameter independently plays the same role in controlling various parts of the radial profile of tangential velocity for a single vortex as for concentric vortices (i.e., tornado embedded in a tornado cyclone).

2) The pressure deficit in a single vortex core has been shown to be sensitive to the shapes of the radial profile of tangential velocity (WW13). For a given tangential velocity peak, a decrease (an increase) in λ narrows (broadens) the profile straddling the maximum by decreasing (increasing) the radial width at a given tangential velocity level. At the same time, it raises (lowers) the corresponding pressure deficit profile and hence fills (deepens) the central pressure deficit. Increasing (decreasing) the μ_i parameter that controls the inner profile not only fills (deepens) the central pressure deficit but also increases (decreases) the central width of the pressure deficit profile inside the radius of the tangential velocity peak. Increasing (decreasing) the μ_o parameter that controls the outer profile deepens (fills) the central pressure deficit.

3) The cyclostrophic balance is partitioned into separate pressure components that correspond to multiple-maxima tangential wind profiles in order to quantitatively evaluate the significant fluctuations in central pressure deficits. Varying any of the parameters (V_x, R_x, μ_i, μ_o, λ) independently plays the same role in controlling various portions of the pressure deficit profile for a single vortex as for concentric vortices.

Acknowledgments. The authors appreciate the helpful comments on this manuscript provided by Chris Karstens of NSSL. The authors thank Jeff Snyder and Howie Bluestein of University of Oklahoma for providing us their RaXPol images shown in Fig. 1.

7. REFERENCES

Burgers, J. M., 1948: A mathematical model illustrating the theory of turbulence. *Adv. Appl. Mech.,* **1,** 197-199.

Davies-Jones, R. P., 1986: Tornado dynamics. *Thunderstorm Morphology and Dynamics*, 2nd ed. E. Kessler, Ed., University of Oklahoma Press, 197-236.

_____, and E. Kessler, 1974: Tornadoes. *Weather and Climate Modification,* W. N. Hess, Ed., John Wiley and Sons, 552-595.

Doswell, C. A., III, H. E. Brooks, and N. Dotzek, 2009: On the implementation of the Enhanced Fujita scale in the USA. *Atmos. Res.,* **93,** 554-563.

Haan, F. L., Jr., V. K. Balaramudu, and P. P. Sarkar, 2010: Tornado-induced wind loads on a low-rise building. *J. Struct. Eng.,* **136,** 106-116.

Karstens, C. D., T. M. Samaras, B. D. Lee, W. A. Gallus, Jr., and C. A. Finley, 2010: Near-ground pressure and wind measurements in tornadoes. *Mon. Wea. Rev.,* **138,** 2570-2588.

Knaff, J. A., C. R. Sampson, P. J. Fitzpatrick, Y. Jin, and C. M. Hill, 2011: Simple diagnosis of tropical cyclone structure via pressure gradients. *Wea. Forecasting,* **26,** 1020-1031.

Lee, W.-C., B. J.-D. Jou, P.-L. Chang, and S.-M. Deng, 1999: Tropical cyclone kinematic structure retrieved from single-Doppler radar observations. Part I: Interpretation of Doppler velocity patterns and the GBVTD technique. *Mon. Wea. Rev.,* **127,** 2419-2439.

Levenberg, K., 1944: A method for the solution of certain problems in least squares. *Quart. Appl. Math.,* **2,** 164-168.

Marquardt, D., 1963: An algorithm for least-squares estimation of nonlinear parameters. *J. Soc. Ind. Appl. Math.,* **11,** 431-441.

Marquis, J., Y. Richardson, J. Wurman, and P. Markowski, 2008: Single- and dual-Doppler analysis of a tornadic vortex and surrounding storm-scale flow in the Crowell, Texas supercell of 30 April 2000. *Mon. Wea. Rev.,* **136,** 5017-5043.

Mishra, A. R., D. L. James, and C. W. Letchford, 2008: Physical simulation of a single-celled tornado-like vortex, Part B: Wind loading on a cubical model. *J. Wind Eng. Ind. Aerodyn.,* **96,** 1258-1273.

Pazmany, A. L., J. B. Mead, H. B. Bluestein, J. C. Snyder, and J. B. Houser, 2013: A mobile rapid-scanning X-band polarimetric (RaXPol) Doppler radar system. *J. Atmos. Oceanic Technol.,* **30,** 1398-1413.

Press, W. H., S. A. Teukolsky, W. T. Vetterling, and B. P. Flannery, 1992: *Numerical Recipes in Fortran 77: The Art of Scientific Computing.* 2nd ed. Cambridge University Press, 933 pp.

Rankine, W. J. M., 1882: *A Manual of Applied Physics.* 10th ed., Charles Griff and Co., 663 pp.

Rott, N., 1958: On the viscous core of a line vortex. *Z. Angew. Math. Phys.,* **9,** 543-553.

Snyder, J. C., and H. B. Bluestein, 2014: Some considerations for the use of high-resolution mobile radar data in tornado intensity determination. *Wea. Forecasting (in press).*

Tanamachi, R. L., H. B. Bluestein, W.-C. Lee, M. Bell, and A. Pazmany, 2007: Ground-based velocity track display (GBVTD) analysis of W-band Doppler radar data in a tornado near Stockton, Kansas, on 15 May 1999. *Mon. Wea. Rev.,* **135,** 783-800.

Tanamachi, R. L., H. B. Bluestein, M. Xue, W.-C. Lee, K. A. Orzel, S. J. Frasier, and R. M. Wakimoto,2013: Near-surface vortex structure in a tornado and in a sub-tornado-strength, convective-storm vortex, observed by a mobile, W-band radar during VORTEX2. *Mon. Wea. Rev.,* **141,** 3661-3690.

Wood, V. T., and L. W. White, 2011: A new parametric model of vortex tangential-wind profiles: Development, testing, and verification. *J. Atmos. Sci.,* **68,** 990-1006.

_____, and _____, 2013: A parametric wind-pressure relationship for Rankine versus non-Rankine cyclostrophic vortices. *J. Atmos. Oceanic Technol.,* **30,** 2850-2867.

_____, _____, H. E. Willoughby, and D. P. Jorgensen, 2013: A new parametric tropical cyclone tangential wind profile model. *Mon. Wea. Rev.,* **141,** 1884-1909.

Wurman, J., and K. Kosiba, 2013: Finescale radar observations of tornado and mesocyclone structures. *Wea. Forecasting,* **28,** 1157-1174.

_____, _____, P. Robinson, and T. Marshall, 2014: The role of multiple-vortex tornado structure in causing storm researcher fatalities. *Bull. Amer. Soc.,* **95,** 31-45.

Yang, Z., P. Sarkar, and H. Hu, 2011: An experimental study of a high-rise building model in tornado-like winds. *J. Fluids Struct.,* **27,** 471-486.

TABLE 1. Model parameters that produced the radial profiles of the secondary vortices in the five experiments. Note that a horizontal arrow represents a change from one parameter value to another. For comparison with these secondary vortices, the initial parameters for generating the primary (reference) Rankine vortex are given as: $V_{px} = 100$ *m s*$^{-1}$, $R_{px} = 0.2$ *km,* $\mu_{pi} = 1$, $\mu_{po} = -1$, *and* $\lambda_p = 0.01$.

Vortex ID	V_{sx}	R_{sx}	μ_{si}	μ_{so}	λ_s
A	25 → 50	2	1	-1	0.01
B	25	2 → 1	1	-1	0.01
C	25	2	1 → 5	-1	0.01
D	25	2	1	-1 → -0.5	0.01
E	25	2	1	-1	0.01 → 1

TABLE 2. Model parameters that produced the radial profile of the primary non-Rankine vortex F. Note that a horizontal arrow represents a change from one parameter value to another. For comparison with the non-Rankine vortex, the initial parameters for generating the primary (reference) Rankine vortex are given as: $V_{px} = 100$ *m s*$^{-1}$, $R_{px} = 0.2$ *km,* $\mu_{pi} = 1$, $\mu_{po} = -1$, *and* $\lambda_p = 0.01$.

Vortex ID	V_{px}	R_{px}	μ_{pi}	μ_{po}	λ_p
F	100	0.2	1	-1	0.01 → 1

TABLE 3. Model parameters that produced the radial profile of the tertiary non-Rankine vortex G. The vortex has been added to the primary and secondary vortices, as shown in FIG 9.

Vortex ID	V_{tx}	R_{tx}	μ_{ti}	μ_{to}	λ_t
G	15	4	1	-1	0.01

TABLE 4. Fitted model parameters for primary and secondary vortices. NA represents not applicable.

Time	V_{px}	R_{px}	μ_{pi}	μ_{po}	λ_p	*RMS*	*CC*	V_{sx}	R_{sx}	μ_{si}	μ_{so}	λ_s	*RMS*	*CC*
2236:31	11.8	61.6	1.17	-1.35	0.69	0.04	1.00	6.4	306.8	6.56	-0.99	1.24	0.12	1.00
2236:48	11.8	100.9	1.00	-1.55	2.21	0.09	1.00	1.3	383.4	17.06	-0.01	0.95	0.11	0.98
2237:06	11.5	151.9	1.28	-3.38	7.56	0.21	1.00	NA	NA	NA	NA	NA	NA	NA

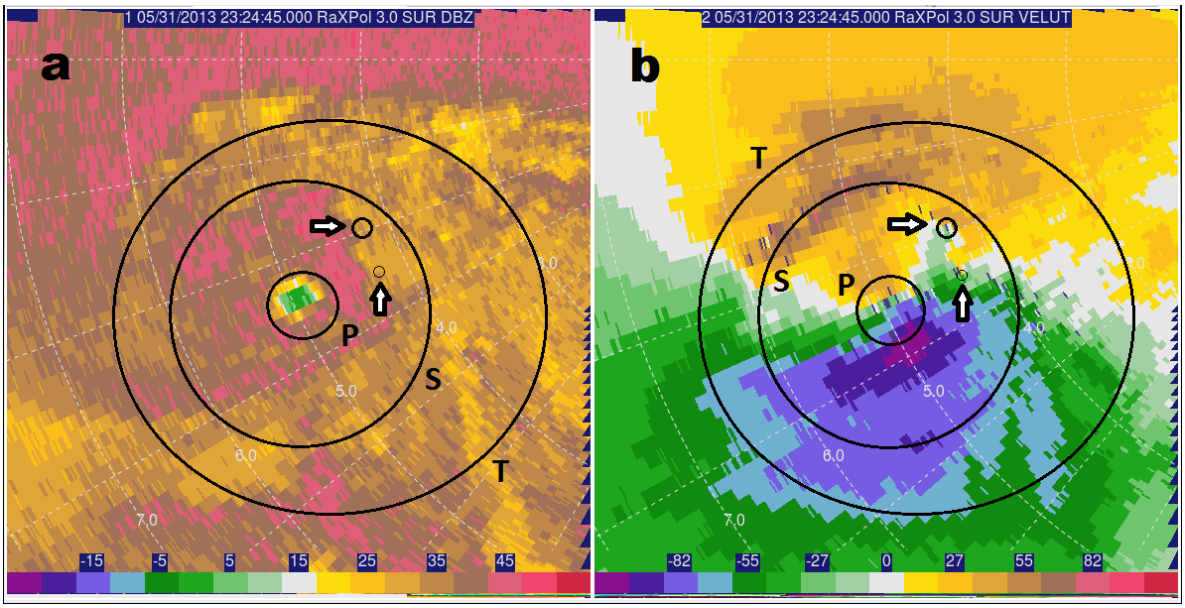

FIG. 1. Fields of (a) RaXPol radar reflectivity (dBZ) and (b) ground-relative Doppler velocity (m s^{-1}) of the El Reno, Oklahoma vortices of 31 May 2013 at 2324:45 UTC. At an elevation angle of 3.0°, beam altitude at a 5-km range from the radar site is 0.26 km AGL. On the Doppler velocity scale, the deficit and maximum values, respectively, are -116 and +116 m s^{-1}. Dashed range rings are marked every 1 km, with dashed spokes provided every 10° in azimuth. Black circles represent approximate core sizes of the primary (P), secondary (S) and tertiary (T) vortices. Very small circles indicated by arrows show the possible presence of satellite vortices. Storm motion is 15 m s^{-1} from 204°. (Data courtesy of J. Snyder and H. Bluestein of University of Oklahoma.)

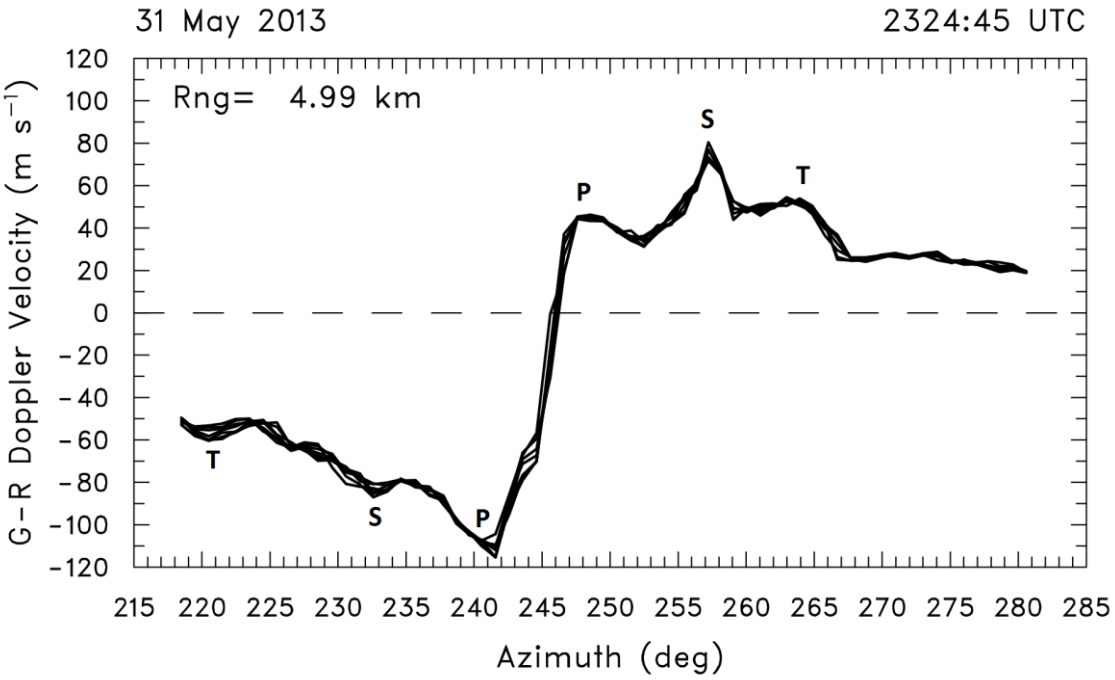

FIG. 2. A few adjacent azimuthal profiles of ground-relative Doppler velocities across the primary vortex signature centered at 5 km at 2324:45 UTC, 31 May 2013. Labels P, S, and T represent the primary, secondary and tertiary vortices, respectively.

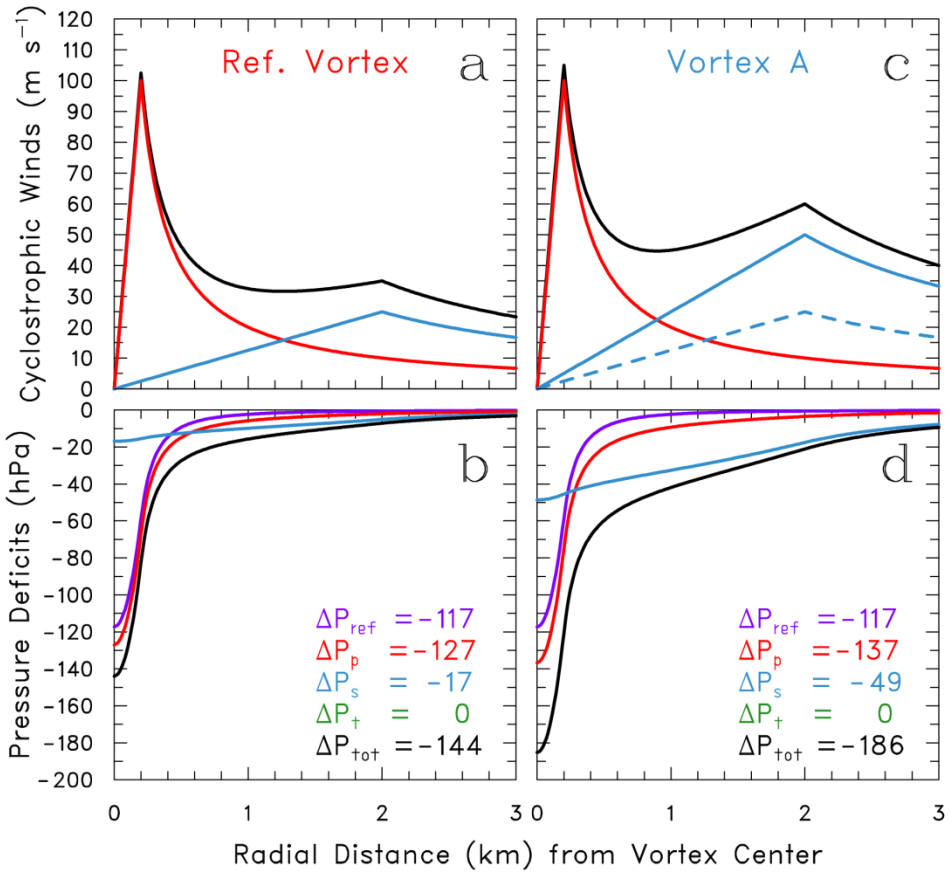

FIG. 3. Radial distributions of (a) and (c) primary V_p (subscript p, red curve), secondary V_s (subscript s, blue curve) and total V_c (subscript c, black curve) cyclostrophic tangential velocities and (b) and (d) corresponding pressure deficits as a function of V_{px}, V_{sx}, μ_{pi}, μ_{si}, μ_{po}, μ_{so}, λ_p, and λ_s. In (a) and (b), the red curve represents a reference (primary) Rankine vortex; the blue curve represents a secondary Vortex A for comparison. The black curve represents the resultant cyclostrophic tangential velocity (V_c) profile resulted when the red primary cyclostrophic tangential velocity (V_p) profile has been added to the blue secondary cyclostrophic tangential velocity (V_s) profile. In (c), the blue dashed curve is the same as the blue solid curve in (a), as discussed in text. In (b) and (d), the purple curve represents a single reference (primary) Rankine vortex's corresponding reference (subscript ref) pressure deficit without being influenced by other secondary vortex. The black curve represents the total pressure deficit ΔP_{tot}. Note that the tertiary (subscript t, green curve) tangential velocity profile is not shown since $V_{tx} = 0$. The constant air density ρ at height of 0.5 km MSL is assumed to be 1.171 kg m^{-3}.

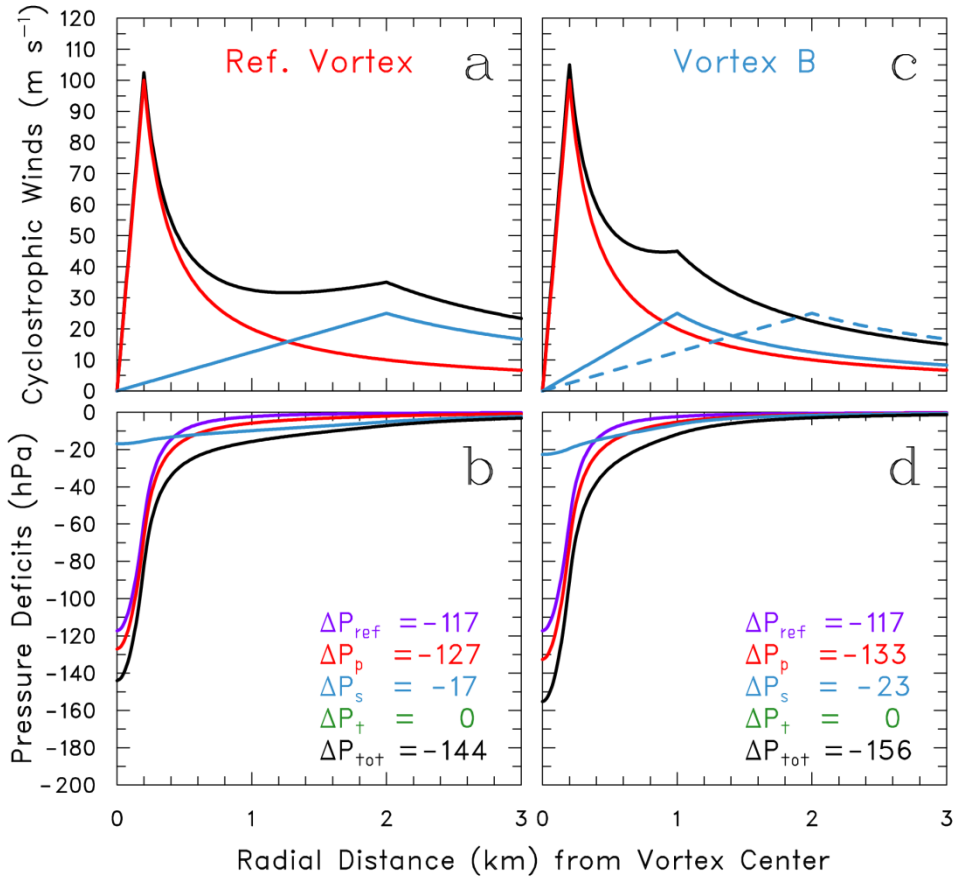

FIG. 4. Same as FIG. 3, except for secondary Vortex B.

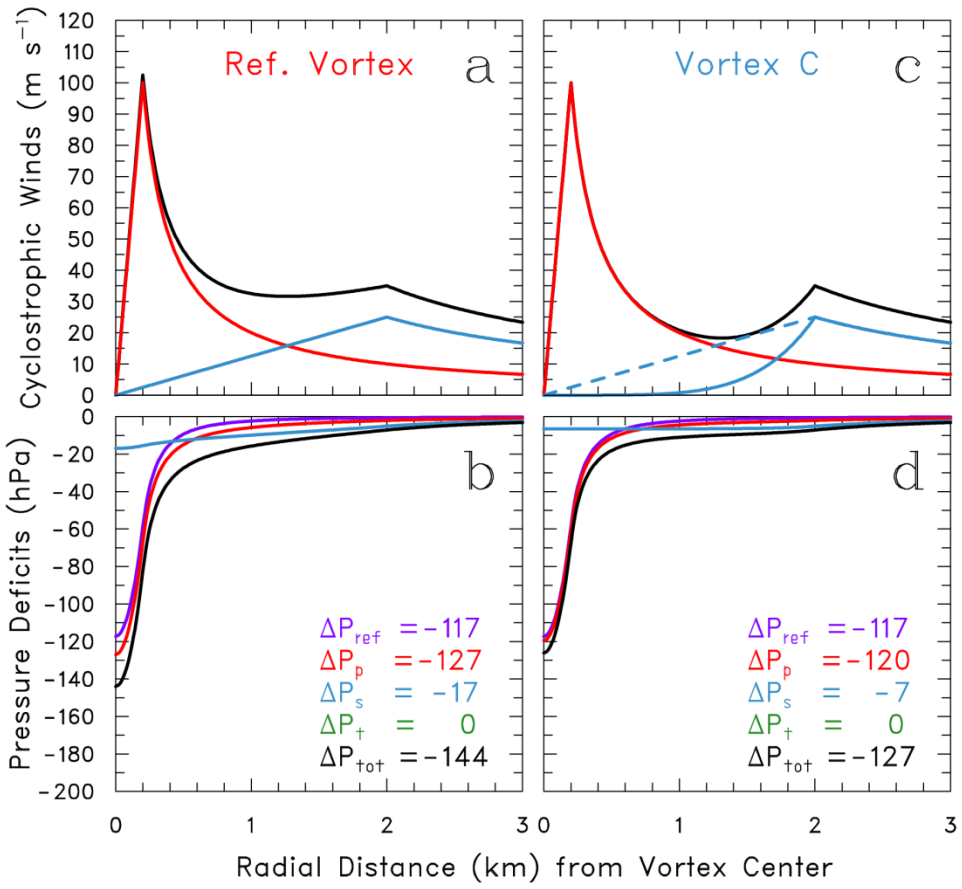

FIG. 5. Same as FIG. 3, except for secondary Vortex C.

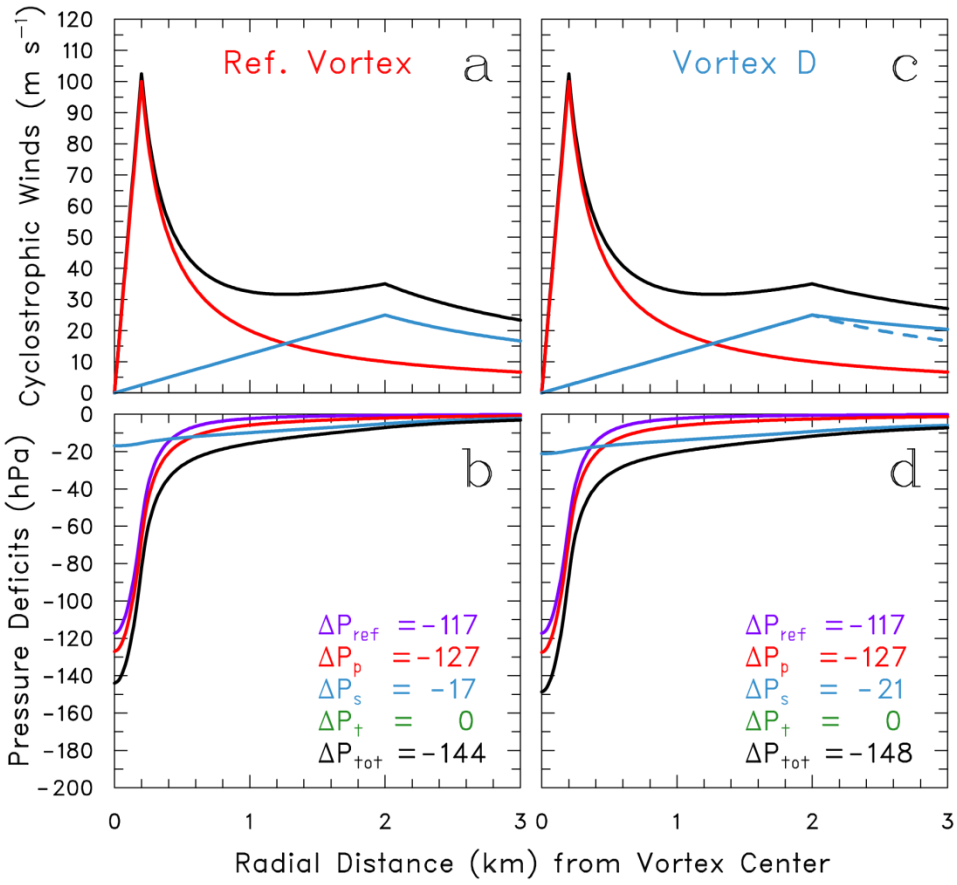

FIG. 6. Same as FIG. 3, except for secondary Vortex D.

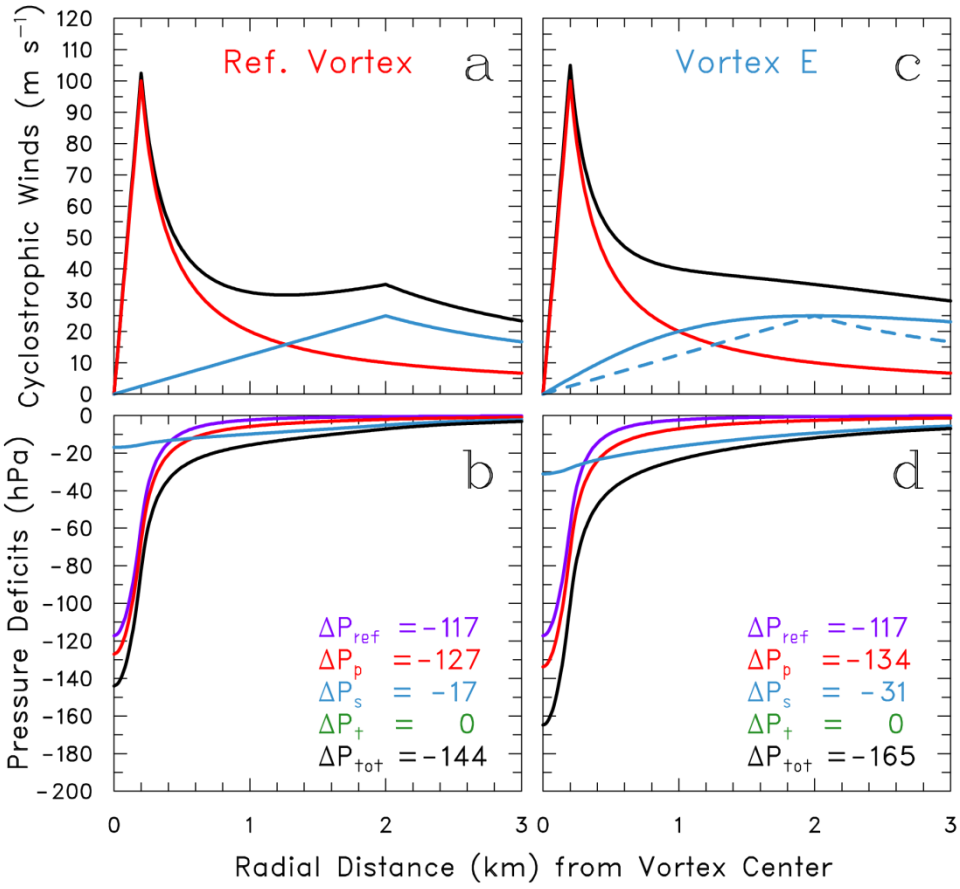

FIG. 7. Same as FIG. 3, except for secondary Vortex E.

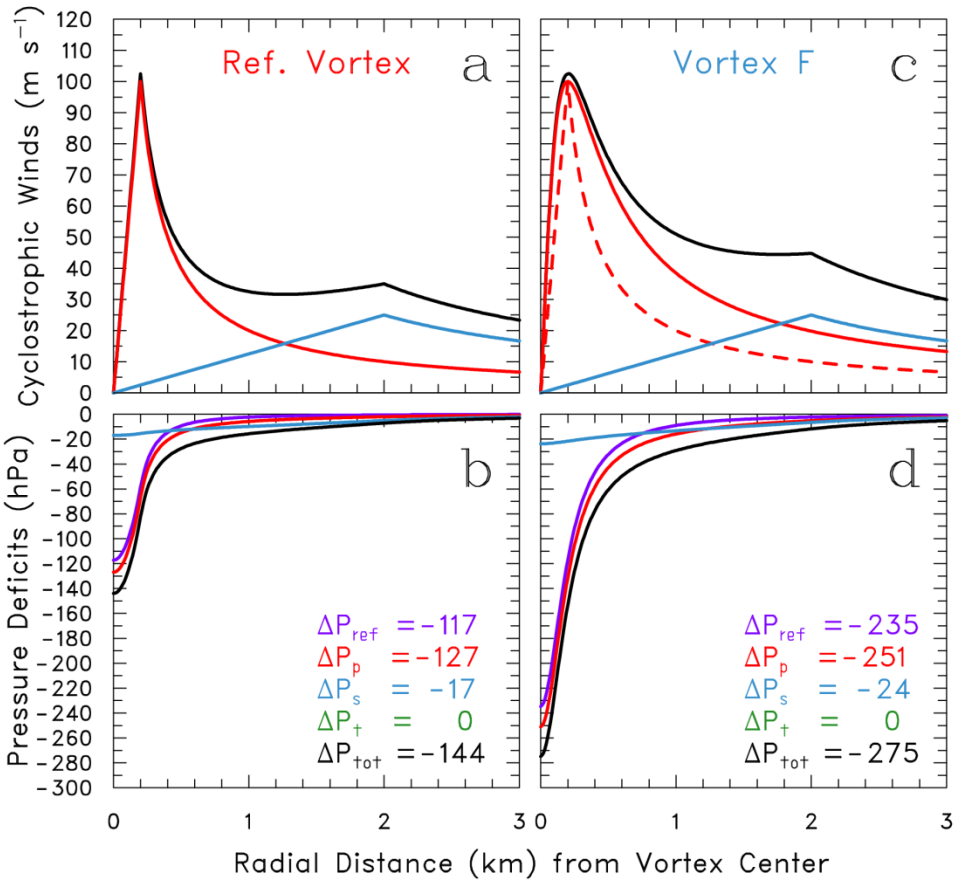

FIG. 8. Same as FIG. 3, except for primary Vortex F. Note that the ordinate scale for pressure deficits is different from that in FIG. 3. In (c), the red dashed curve is the same as the red solid curve in (a).

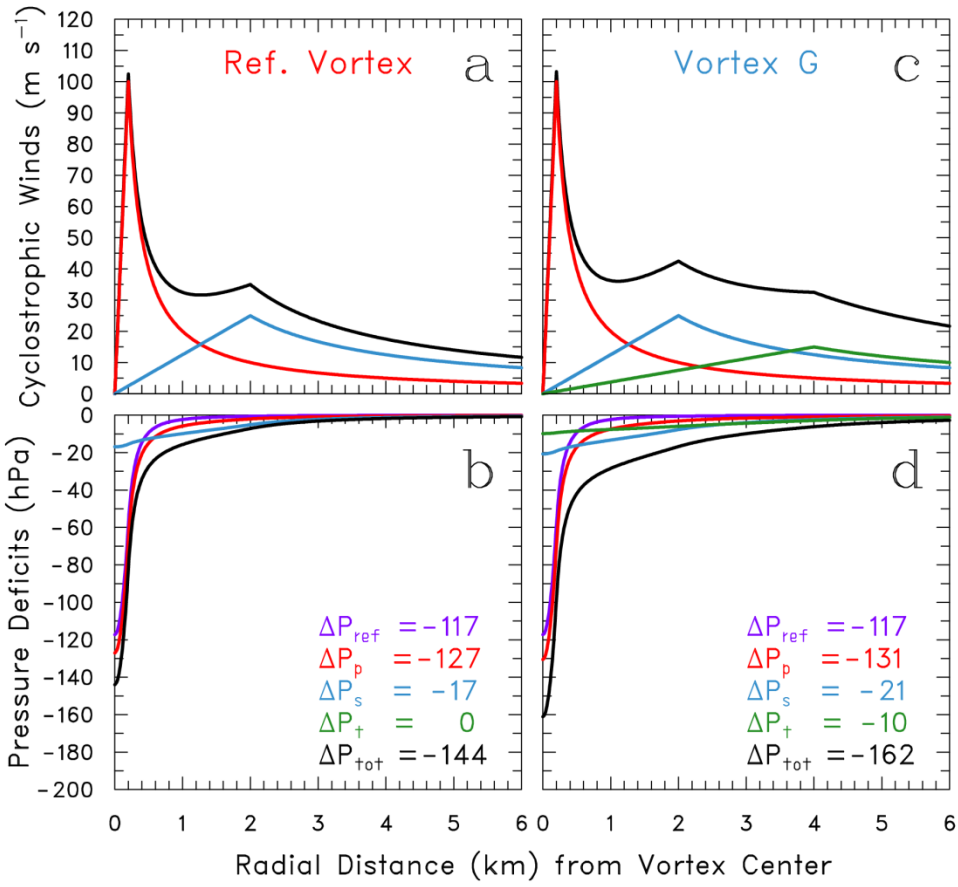

FIG. 9. Same as FIG. 3, except for tertiary Vortex G. The abscissa scale for radial distance has been extended to depict the radial profile (green) of the tertiary vortex's tangential velocity

FIG. 10. UMass W-band reflectivity (filled color contours, dBZ_e) and GBVTD-analyzed, vortex-relative, asymmetric azimuthal velocities (sum of wavenumbers 0-3, in black contour interval of 2 m s^{-1}) for the Prospect Valley, Colorado SCV of 26 May 2010 at (a) 2236:31, (b) 2236:48, and (c) 2237:06 UTC at height of 150 m AGL. The abscissa and ordinate scales for radial distance (m) from vortex center are indicated. (After Tanamachi et al. 2013.)

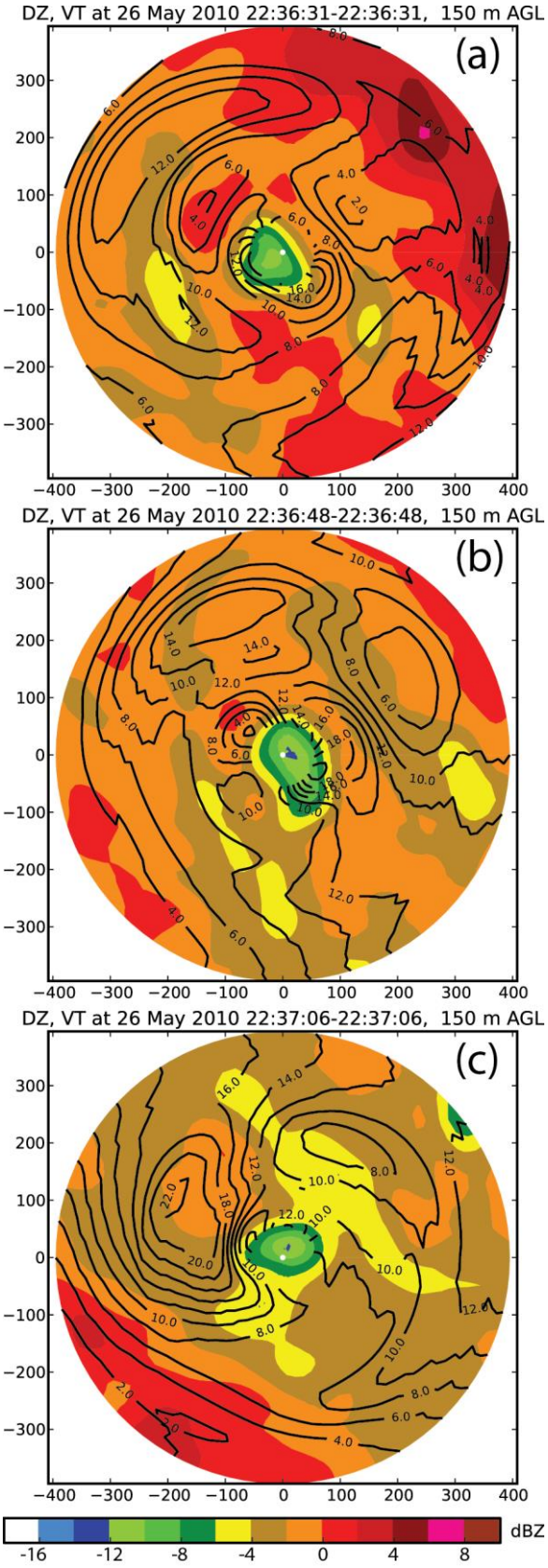

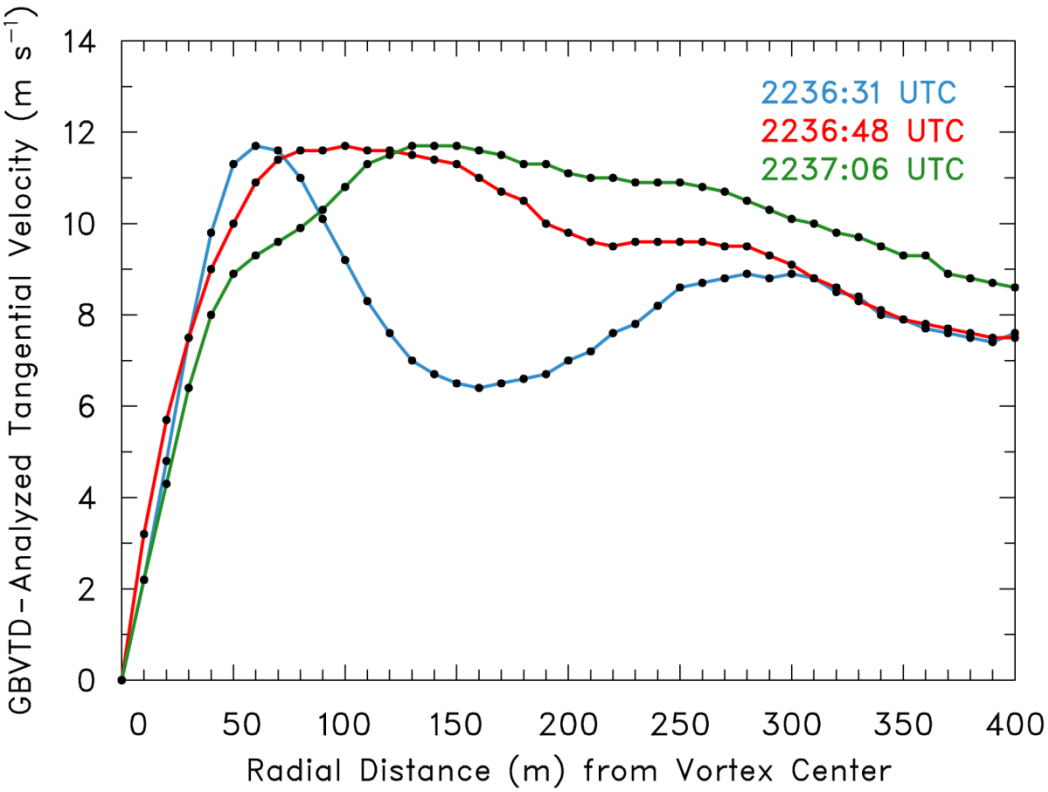

FIG. 11. Radial profiles of GBVTD-analyzed axisymmetric component of tangential velocity for the Prospect Valley, Colorado SCV of 26 May 2010 at 2236:31 (blue), 2236:48 (red) and 2237:06 (green) UTC at height of 150 m AGL. Black dots represent data points every 10 m. (After Tanamachi et al. 2013.)

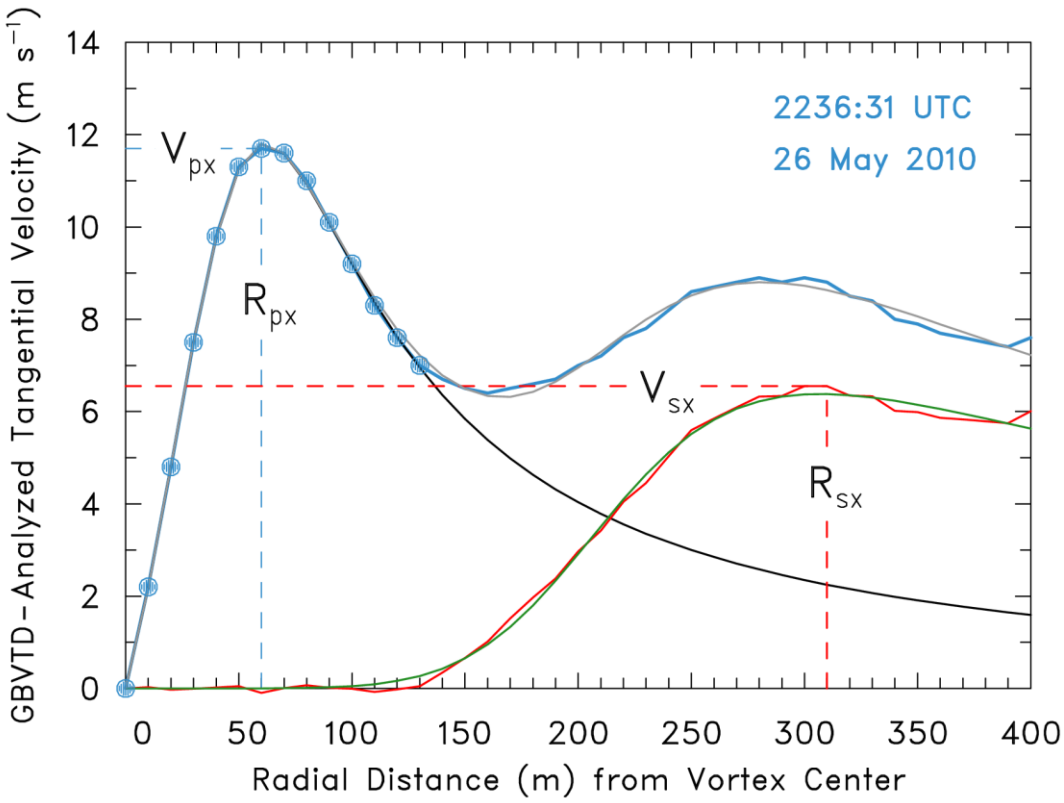

FIG. 12. Radial profiles of GBVTD-analyzed and fitted tangential velocity for the primary and secondary vortices at 2236:31 UTC, 26 May 2010. Blue dotted line represents data points to be minimized in the cost function. Locations of initial guesses of V_{px}, R_{px}, V_{sx}, and R_{sx} are indicated.

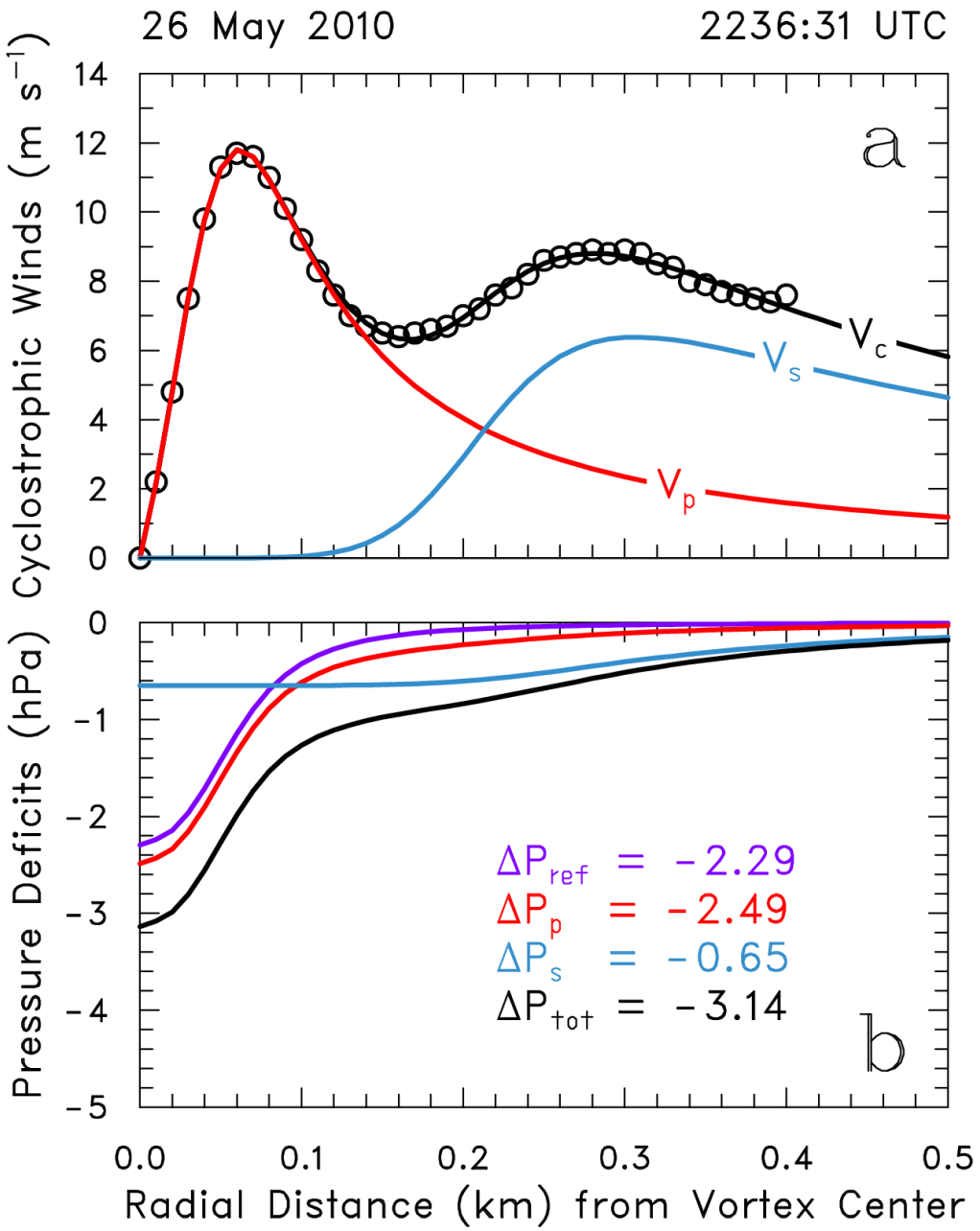

FIG. 13. (a) Radial profiles of fitted tangential velocity for the total (black), primary (red) and secondary (blue) cyclostrophic vortices at 2236:31 UTC, 26 May 2010. The black circles refer to the observed data points. (b) Radial profiles of pressure deficit deduced from the fitted tangential wind profiles in (a).

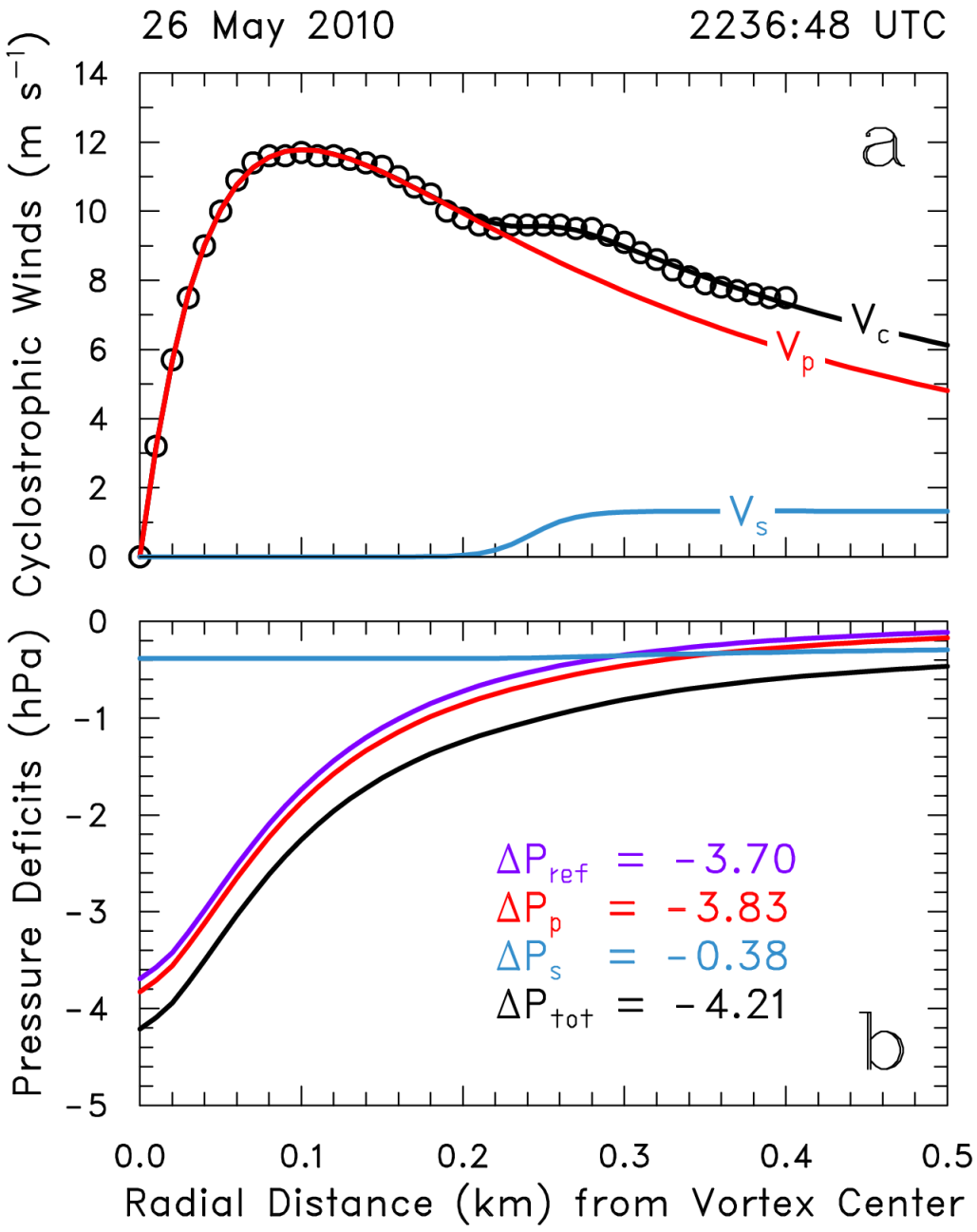

FIG. 14. Same as FIG. 13, except for 2236:48 UTC.

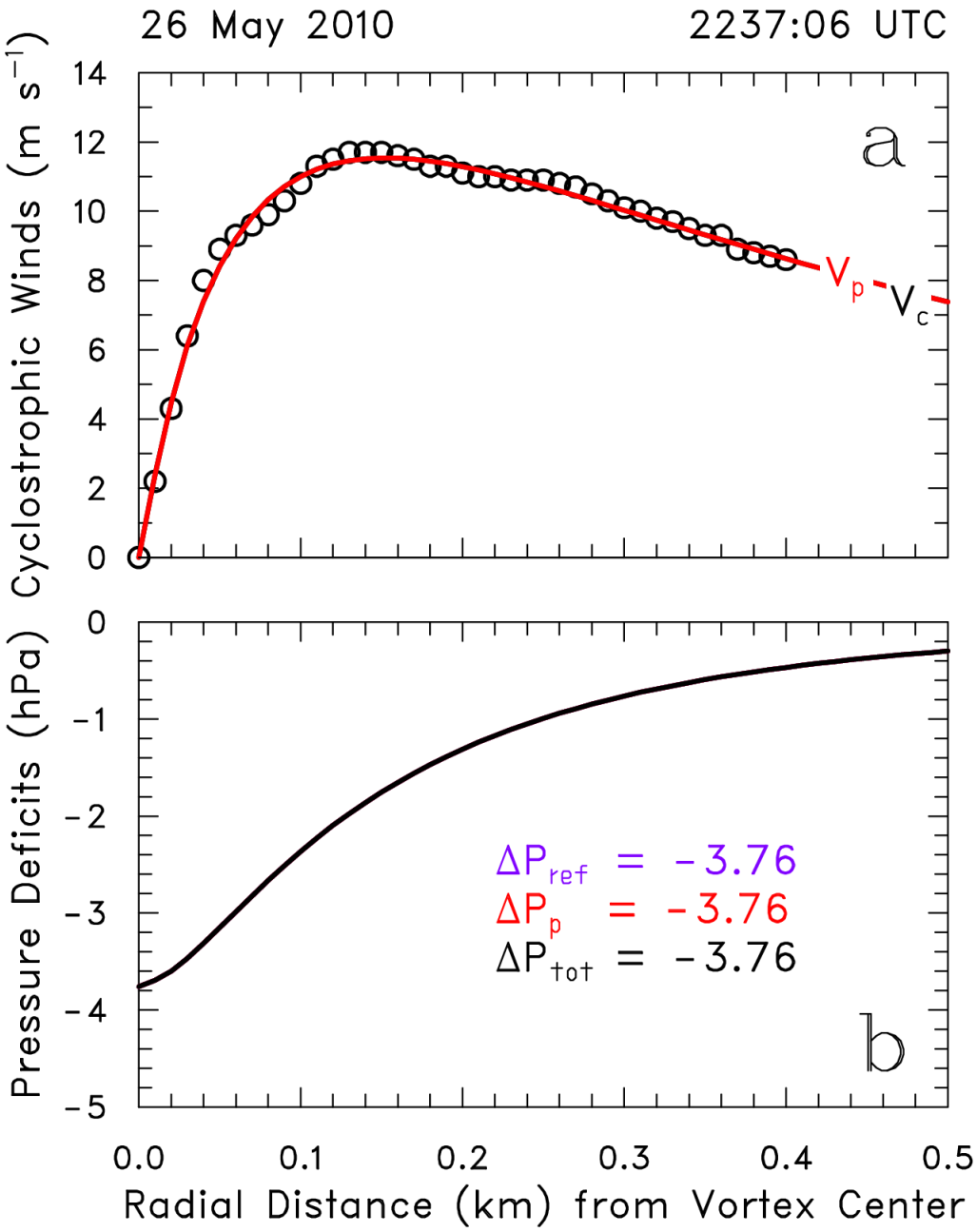

FIG. 15. Same as FIG. 13, except that only single radial profile of fitted tangential velocity for the total (primary) cyclostrophic vortex at 2237:06 UTC, 26 May 2010.